Timescale of Antarctic Ice Shelf Collapse via Crevassing

A. T. Bradley[1], C. Y. Lai[2], N. Coffey[2]

[1]British Antarctic Survey, Cambridge, UK

[2]Department of Geophysics, Stanford University, CA, USA

Corresponding author: Alexander T. Bradley, aleey@bas.ac.uk

Abstract

Antarctic ice shelves are known to be vulnerable to collapse, but when this might happen is largely unknown, propagating significant uncertainty into sea level rise projections. To help to constrain this, we consider two questions: firstly, under current conditions, how long might it take for ice shelves to collapse due to crevassing and, secondly, how might these timescales change under future warming? Using a linear elastic fracture mechanics framework, combined with realistic ice temperature profiles, we identify timescales of collapse of all Antarctic ice shelves. We reveal a strong sensitivity of the ice shelf collapse timescale on basal melt rates, through a combination of the effect of basal melting on the ice temperature profile, ice shelf strain rates, and ice shelf thinning rates. We find that, on the one hand, ice shelves with high basal melt rates, such as those in West Antarctica, typically have short (10s-100s of years) collapse timescales, demonstrating their vulnerability to collapse in the coming century. On the other hand, ice shelves with low basal melt rates, such as the Ross and Ronne-Filchner ice shelves, have extremely long (10,000s years) timescales, suggesting that their current configurations are highly stable. We find, however, that these collapse timescales reduce dramatically with increases in basal melting. Under medium-to-high emmissions scenarios, collapse timescales on these currently stable ice shelves reduce to 100s of years by the end of the century. These results have significant implications for committed and future sea level rise from the Antarctic Ice Sheet and point towards a higher ice-ocean sensitivity than previously understood.

Introduction

Ice shelves – the floating extensions of grounded ice sheets – apply a backstress (or 'buttressing') to the flow of upstream grounded ice sheets (Fürst et al., 2016; Reese et al., 2018; Gudmundsson et al., 2012). This stress restrains their flow, thereby modulating sea level rise contributions. Recent evidence suggests that large areas of the ice shelves fringing the Antarctic ice sheet are vulnerable to collapse (Lai et al., 2020), including large swathes which provide significant buttressing (Fürst et al., 2016). However, these vulnerability estimates lack a timescale on potential ice shelf collapse. This is pertinent because the question of *when* ice shelves will collapse represents a significant uncertainty on future sea level rise: current estimates (Edwards et al., 2021; Seroussi et al., 2020; Bett et al., 2023; DeConto et al., 2021; Coulon et al., 2023) suggest that sea level rise from Antarctica over the next century will be on the order of 10s of centimeters if ice shelves

remain intact. However, simulations in which ice shelves are removed, either by runaway cliff collapse (DeConto & Pollard, 2016) or instantaneously (Sun et al., 2020), project sea level rise on the order of meters over the same time period. To help to constrain these uncertainties, here we consider two questions: firstly, under current conditions, what are the timescales associated with ice shelf collapse due to crevassing, and secondly, how might these timescales change under future warming?

Results

Ice shelf crevassing is sensitive to basal melting

To probe these questions, we first consider the effect of internal ice temperatures on ice shelf crevassing, since ice temperatures are a first order control on ice shelf rifting (Lai et al., 2020; Coffey et al., 2023). Over the Antarctic ice sheet, advection, rather than diffusion, dominates heat transfer (supplementary figure 5); under this condition, the temperature within ice-shelves can be approximately expressed (Sergienko et al., 2013) as (methods)

$$T(x,\hat{z}) = T_g(\hat{z}) + T_d(x)\exp\left(-\frac{\hat{z}}{\ell}\right), \qquad \ell = \frac{\kappa}{\dot{m}H}. \tag{1}$$

Here, x is the along flow co-ordinate (figure 1a), $\hat{z}(x) = z/H(x)$ is a dimensionless vertical co-ordinate, with $z = 0$ at the ice shelf base, $H = H(x)$ is the ice thickness, $T_g(\hat{z})$ is the temperature at the grounding line, κ is the ice diffusivity, and $\dot{m}$ is the basal melt rate. $T_d > 0$ is a vertical diffusive term, which allows the basal boundary condition – that the ice must be at the local freezing point – to be satisfied. Although the thermal structure of Antarctic ice shelves has not been studied extensively, both modelling (Wang et al., 2022; Grosfeld & Thyssen, 1994) and borehole observations (Wang et al., 2022; Eicken et al., 1994; Kobs et al., 2014; Tyler et al., 2013) support the temperature profile (1) (methods).

The temperature profile (Robin, 1955), indicates that ice temperatures are warmest at the base, transitioning to cold surface temperatures across their thickness (figure 1a). The local basal warming effect is confined to a region of dimensionless thickness ℓ (equation (1)). In ice shelves with higher basal melt rates (lower ℓ), this basal warming region is narrower, and temperatures transition to the colder surface temperatures over

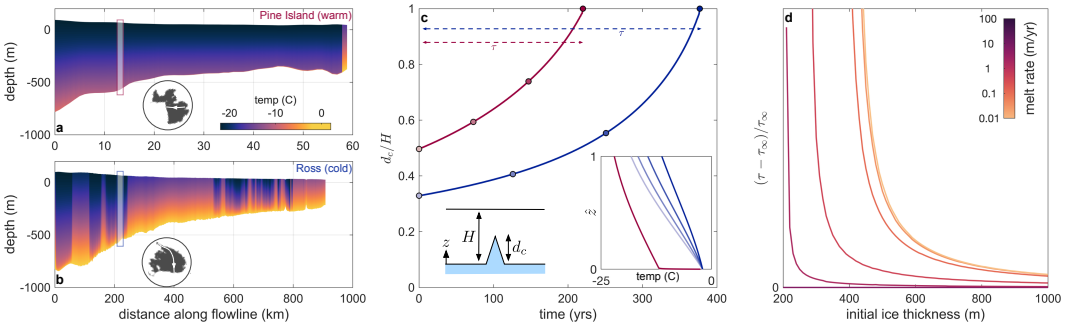

Figure 1. Basal melt rates strongly influence LEFM crevasse time. (a,b) Analytic temperature profiles (methods) along flowlines (inset) taken from the central portion of (a) the Pine Island Ice Shelf and (b) the Ross Ice Shelf (b). In both cases, the melt rate used to determine the ice temperature is from satellite observations (Adusumilli et al., 2020). (c) Dimensionless crevasse depth predicted by LEFM as a function of time for the column of ice in panel a (red) and panel b (blue), which is forced to thin under a constant thinning rate of 1 m/year. In both cases, the column of ice has initial thickness 600 m and other parameters are identical, i.e. the only difference between the two cases in the basal melt rate (in particular, the thinning and strain rates are artificially adjusted to be identical, and not in line with observations, to highlight the effect of the ice temperature on the crevasse time). The quantity τ is the crevasse timescale, the time taken for the crevasse to propagate through the thickness of the ice shelf, as indicated by the dashed arrow. Inset: evolution of the temperature profile for the Ross Ice Shelf column (blue hues) and Pine Island Ice Shelf column (red hues), with darker curves corresponding to later times, as indicated by points in the main panel. Note that the red hues are almost indistinguishable, indicating that the temperature profile does not change significant during the thinning. (d) Plot of $(\tau - \tau_c/\tau_c)$, the enhancement of crevasse time over that with a very high melt rate (in this with case $\dot{m} = 250$ m year^{-1}), denoted τ_c as a function of initial column thickness. Different curves correspond to different melt rates, as indicated by the colourbar.

a shorter distance, compared to ice shelves with relatively low basal melt rates (figure 1a, b). As a result, ice shelves with high basal melt rates tend to have colder ice; colder ice is more brittle (LeB. Hooke, 1981), promoting larger crevasses, so higher basal melt rates promote larger crevasses. Figure 1c (at time = 0) shows that, under identical conditions except for different ice temperatures, basal crevasse depths as determined by linear elastic fracture mechanics (LEFM, methods) are smaller on a flowline from the Ross ice shelf (low basal melt rate) than on a flowline from Pine Island Ice Shelf (high basal melt rate).

To facilitate an assessment of the timescale associated with crevassing, we construct a crevassing timescale, τ, which is the time taken for a crevasse to propagate through a column of ice, which is thinned under a given thinning rate (figure 1c, and methods). As a column of ice thins, the resistive stresses required to open a fracture reduces (methods), promoting increased crevasse depths. This is modulated by the basal warming region becoming wider as the column thins (H reduces, see equation (**??**)), promoting increased ice shelf temperature and thus reduced crevasse depths. With a low basal melt rate, the temperature profile adjusts significantly during the thinning (inset in figure 1c), whereas with a high basal melt rate, changes in the temperature profile are minor, i.e. the stabilizing effect of a changing ice temperature with thinning only plays a role for low melt basal melt rates. Not only does the crevasse begin (i.e. before any thinning) shallower for a low basal melt rate, but the stabilizing effect of changes in ice temperature profile throughout thinning is greater. As a result, the crevassing timescale in areas with a high basal melt rate may be much shorter than with a low basal melt. In the example shown in figure 1, the crevassing timescale τ is approximately 80% longer for the low basal melt rate case, under otherwise identical conditions. For other values of the basal melt rate and initial ice thickness, the crevassing timescale may be enhanced by as much as 500%, compared to a very high melt rate case (figure 1c).

In addition to the ice temperature, basal melt rates also affect ice shelf strain rates and thinning rates, which feed back on crevasse depths. LEFM crevasse depths are highly sensitive to ice shelf strain rates (Lai et al., 2020), with higher strain rates promoting increased crevasse depths. Ice has a strain thinning rheology, with higher strain rates resulting in reduced viscosity and thus more brittle ice, which is more liable to crevasse. For Antarctic ice shelves, strain rates increase strongly with melt rates ($p < 0.001$, figure 2a). Although the relationship between strain rates and basal melt rates is complex, depending on the entire ice-sheet system, higher melt rates generally reduce ice shelf buttressing, increasing ice sheet flow speeds and thus strain rates. Additionally, melt rates are highly correlated with thinning rates ($p < 0.001$, figure 2b). Increased thinning rates promote reduced crevassing timescales because a column of ice reaches the critical thickness at which a crevasse will propagate through its thickness sooner. Although the relationship between thinning rates and melt rates is more direct than between melt rates and strain rates (both melt rates and thinning rates appear explicitly in the ice shelf conservation of mass equation), flow divergence modulates the relationship between these

terms. The crucial point is that increases in basal melt rates on ice shelves not only reduce expected crevasse timescales via changes in ice temperature, but also via increases in ice shelf strain rates and thinning rates. Thus, a strong dependence of crevasse timescales on basal melt rates is to be expected.

Circum-Antarctic crevassing and collapse timescales

Figure 3a shows circum-Antarctic crevasse times, determined using observational estimates of ice shelf basal melt rates (Adusumilli et al., 2020), thinning rates (Smith et al., 2020), thickness (Fretwell et al., 2013), and strain rates derived from a data-constrained flow model [Yao - what is the correct reference for Wearing's strain rates], and evaluated on a 1km grid (methods). This map that crevasse timescales are highly sensitive to basal melt rates: areas with high ocean heat content, and thus high basal melt rates, generally have much shorter crevassing times than those areas with low ocean heat content. On a broad scale, crevassing times are generally shortest in the Amundsen and Bellingshausen Sea sectors, where maximum thermal forcing is above 4 °C, while in the Weddell and Ross Seas, thermal forcing is low (¡2 °C) and crevassing times on adjacent ice shelves are generally very long. There are, however, significant heterogeneities on a more local level: for example, crevassing times on the Larsen ice shelves, which are exposed to locally elevated thermal forcing, are much shorter than on the neighbouring Ronne ice shelf, despite both being located in the Weddell Sea sector.

To go beyond these qualitative comparisons, we determine a 'collapse timescale', obtained as the mean of a kernel density estimate of crevassing times over each ice shelf (figure 3b). The collapse timescale is interpreted as the timescale on which these ice shelves will persist, and we stress at the outset that this quantity is not a detailed prediction of when ice shelves will collapse, but rather represents the timescale on which ice shelf loss is expected. Collapse timescales are strongly dependent on basal melt rates (the colour gradient from left to right in figure 3b and supplementary figure 11; High melt rate ice shelves (red in figure 2 and figure 3b), particularly those in the Amundsen Sea sector, have the lowest collapse timescales, which is concomitant with high ocean forcing and basal melt rates. Many of these ice shelves have collapse timescales below 100 years, which supports recent suggestions that many have already been preconditioned for collapse (Lhermitte et al., 2020). Note that the rapidly retreating Thwaites Glacier has the lowest collapse timescale – 8 years – but this number should be taken with caution owing to the dearth

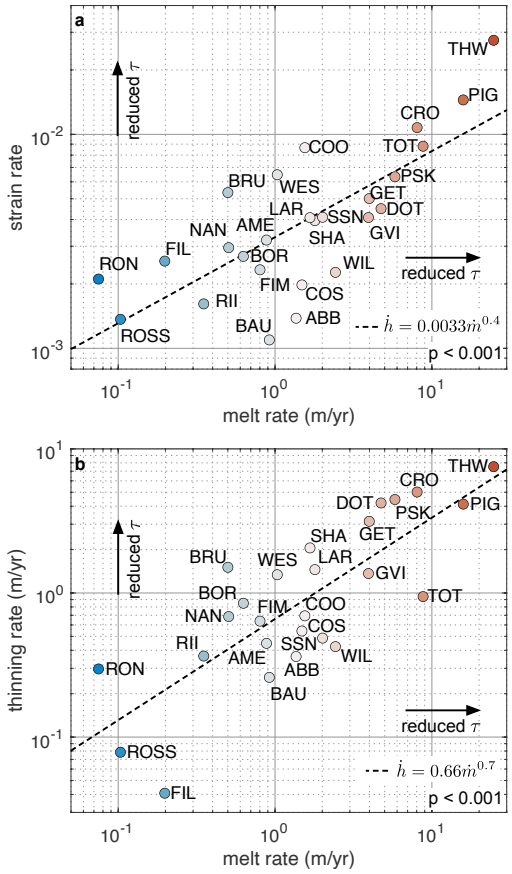

Figure 2. Thinning rate and strain rate are highly correlated with basal melt rates on Antarctic Ice Shelves. Scatter plots of ice shelf average melt rate against (a) ice shelf average strain rate and (b) ice shelf average thinning rate. For each quantity, the average is determined as the arithmetic mean over all ice shelf points. In (a), the black dashed line indicates the best linear fit to the logarithm of both quantities (for example, in (a), the dashed line is the best linear fit of log melt rates against log strain rates, see methods). In both panels, black arrows indicate the direction of reduced crevassing time. Here, ice shelf names are abbreviated as follows: ABB - Abbot; AME - Amery; BAU - King Baudoin; BOR - Borchgrevink; BRU - Brunt; COS - Cosgrove; COO - Cook; CRO - Crosson; DOT - Dotson; FIL - Filchner; FIM - Fimbul and Jelbart (combined); GET - Getz; GVI - George VI; LAR - Larsen; NAN - Nansen; PIG - Pine Island; PSK - Pope, Smith and Kohler (combined); RII - Riiser Larsen, RON - Ronne; ROSS - Ross; SHA - Shackleton; SSN - Swinburne; Sulzberger and Nickersen (combined); THW - Thwaites; TOT - Totten and Moscow University (combined); WES - West; WIL - Wilkins.

of data available for this ice shelf. Although the buttressing effect of these ice shelves varies – for example, the Pine Island ice shelf is thought to provide strong buttressing

of ice upstream (A. T. Bradley et al., 2023), whereas the Thwaites Ice Shelf is thought to only provides limited buttressing (Gudmundsson et al., 2023) – models unanimously agree that ice shelf loss in the Amundsen Sea sector will result in high sea level rise (Sun et al., 2020) from this sector; our results suggest ice shelves in the Amundsen sea sector will likely be lost by the end of the century even under present day conditions. This supports the suggestion that a significant sea level rise contribution from the West Antarctic Ice Sheet before the end of the century is already committed. At the other end of the spectrum, the Amery, Ronne, Ross, and Filchner ice shelves have collapse timescales on the order of thousands of years, suggesting that, under current conditions, these ice shelves are very stable: if current conditions persist, these ice shelves will continue to buttress their large inland sectors, limiting their sea level rise contributions.

One outlier in this picture are the Totten and Moscow University ice shelves, which, despite very high basal melt rates (figure 2a), display long collapse timescales. This is a result of their relatively thick ice (supplementary figure 10d) and low thinning rates, which are several times smaller than other ice shelves with similar melt rates (figure 2b). At the other end of the spectrum, the Brunt ice shelf displays anomalously low collapse times, resulting from its relatively high strain (figure 2a) and thinning (figure 2b rates. We note, however, that this short Brunt timescale is consistent with significant calving which took place in January 2023 (Marsh et al., 2023).

It is interesting to compare collapse timescales obtained using LEFM with those from Nye theory (Nye, 1957) and more recent updates (Coffey et al., 2023). These collapse timescales are obtained using the same procedure as outlined above, but with crevasse depths at each timestep calculated using the relevant theory (methods). We find that, regardless of the crevasse depth theory used, the collapse timescale remain on the same order of magnitude, and strongly dependent on the melt rate, supporting the conclusions made herein (figure 3b). It is interesting to note that collapse timescale computed using Nye theory are always larger than those obtained using LEFM. This suggests that ice sheet models which parametrize damage or calving using Nye theory (Sun et al., 2017) may underestimate future ice shelf loss and thus sea level rise contributions.

Collapse timescales under future warming

The collapse timescales identified in the previous section are appropriate in the case that ice shelf melt rates, strain rates, and thinning rates remain constant in time. In practice, however, these will respond to increasing anthropogenic emissions. To assess the sensitivity of collapse timescales to future warming, we repeat the simulation presented in figure 3 a uniform increases in melting, $\Delta\dot{m}$, applied to the ice shelf. To account for the concomitant increase in strain and thinning rates with melt rates (figure 2), we simultaneously increase these quantities in line with best fits to the relationship between them (black dashed lines in figure 2, methods).

Plots of collapse timescale as a function of $\Delta\dot{m}$ reveal a highly sensitive dependence on future increases in melt rate (note that the y axis is figure 4 is logarithmic). A uniform increase in melt rate of 1 m my^{-1} leads to a larger than 50% reduction in the collapse timescale for each ice shelves with collapse timescales above 100 years under present conditions. Under a 10 m my^{-1} uniform increase in basal rates, the collapse timescale of every ice shelf is reduced by at least an order of magnitude.

To place these results in a realistic context, we use output of a coupled atmosphere-ocean-ice-sheet model (Park et al., 2023) to determine plausible future increases in melt rates and compute associated collapse timescales (methods). The results (figure 4b–e) reveal that the collapse timescale associated with end-of-century melt rates is highly sensitive to the emission pathway, albeit with variations between individual ice shelves. For the Ross ice shelf, collapse times remain on the order of millennia under SSP1-1.9, but reduce dramatically to decadal-to-centennial timescales under SSP2-4.5 and SSP5-8.5. Under SSP1-1.9, Filchner ice shelf collapse times increase by 2100, consistent with other modelling studies which suggest reductions in melting of this ice shelf under low future warming (Nicholls, 1997; Naughten et al., 2021). However, under moderate or severe warming, the Filchner Ice Shelf collapse timescale similarly reduces sharpy. Collapse timescales for the Ronne and Amery Ice Shelves are both reduced by a factor of approximately one-third under SSP1-1.9, with collapse timescales under SSP5-8.5 an order of magnitude smaller than present day values. These results suggest that, while ice shelves with low basal melt rates appear to be very stable at present, future warming may dramatically reduce their stability, with this reduction strongly dependent on the emissions pathway taken.

Discussion

There are three key results of our study: firstly, ice shelves with high basal melt rates have collapse timescales of 10s-100s of years, suggesting they are likely preconditioned to collapse, or lose significant area, before the end of the century, suggesting committed sea level rise; secondly, low basal melt rate ice shelves, particularly the Ross, Ronne, and Filchner ice shelves which buttress large swathes of the Antarctic Ice Sheet, are highly stable in their present configurations, limiting their sea level rise potential; finally, the timescales of loss of ice shelves is extremely sensitive to future increases in basal melt rate, with the large ice shelves potentially preconditioned to collapse by 2100. How these timescales respond in practice is strongly dependent on the emissions pathway, stressing the need for urgent emissions reduction to promote the longevity of Antarctic ice shelves and thereby limit sea level rise from Antarctica. More generally, we have also revealed a previously unreported sensitive dependence of ice shelf collapse on basal melt rates, providing a mechanistic understanding which supports observational studies (Liu et al., 2015) linking increases in basal melt rates with increases in ice shelf calving. Our results also highlight the need for continued and improved observational estimates of key ice sheet indicators, particularly basal melt rates.

We stress that the collapse timescales reported here do not represent a detailed assessment of when ice shelves are expected to collapse, but rather a timescale associated with their persistence. Determining exactly when ice shelves might calve or collapse requires the use of an ice sheet model with a calving law, since removal of sections of the ice shelf will feed back on ice shelf flow, via a reduction in buttressing. As noted, reductions in buttressing are associated with increased strain and thinning rates, and therefore this feedback may reduce the collapse timescales reported in this paper. Loss of sections of ice shelf also have the potential to affect ice shelf basal melt rates (A. Bradley et al., 2022), potentially further reducing collapse timescales. However, on the timescales reported here, grounding lines – where the ice transitions from grounded to floating – of ice sheets may change; where the grounding line is retreating, new sections of ice shelf would be exposed, potentially providing additional buttressing, increasing collapse timescales.

It is also important to acknowledge limitations resulting from assumptions made herein. We have assumed a uniform ice shelf basal temperature, surface temperature, and geothermal heat flux in the temperature profile used (methods). In practice, geother-

mal heat flux rates are elevated around West Antarctica (Fisher et al., 2015); in our framework, this would lead to warmer ice, with reduced crevasse depths, enhancing collapse times in the region. The ice temperature profile also does not account for isothermal marine ice, which is prevalent on some ice shelves (Wang et al., 2022). In addition, we have assumed that each ice column evolves independently of its neighbours and that narrow crevasses (smaller than the 1km grid resolution we use) may be parameterized in this way. Evidence from the collapse of the Larsen C Ice Shelf suggests that propagation of crevasses through the entire thickness of an ice shelf can alter the surrounding stress field, promoting further crevassing (Robel & Banwell, 2019). Furthermore, we have considered only basal crevasses, and assumed that sufficient defects are present in the ice to initiate crevasses (Lai et al., 2020). Basal crevasses tend to be larger than surface crevasses in the LEFM framework owing to the water pressure within them (Lai et al., 2020); including surface crevasses into the framework, which may grow and join basal crevasses, may reduce collapse timescales. However, recent evidence suggests that basal and surface crevasses can interact to suppress their mutual propagation, owing to the moments generated by crevasses (Zarrinderakht et al., 2023), while buoyancy forces may also suppress crevasse propagation (Zarrinderakht et al., 2022)).

Using an LEFM framework, we have shown that high melt rates promote reduced timescales of ice shelf collapse via crevassing through a combination of changes in ice temperature, and increases in both thinning and strain rates. We have produced a circum-Antarctic map of collapse timescales, demonstrating this sensitive dependence in practice. These timescales are dramatically reduced by 2100 under moderate-high emissions scenarios. Our results stress the need for urgent action to reduce the effects of climate change on Antarctica and thus sea level rise contributions.

Data Availability

Code to perform simulations and produce the figures contained in this paper is held in an open GitHub repository: `https://github.com/alextbradley/Collapse-Timescale`.

Methods

Ice shelf temperature profiles

In general, assuming that viscous heating is negligible, internal ice temperature $T(x, y, z, t)$ satisfy the heat equation

$$\frac{\mathrm{D}T}{\mathrm{D}t} = \nabla \cdot (\kappa \nabla T) \tag{2}$$

where t represents time, *kappa* is the thermal diffusivity of ice, and (x, y, z) are a co-ordinate system, with z the vertical co-ordinate. Since ice sheets have high aspect ratios, derivatives with respect to z, are many times larger than those with respect to horizontal co-ordinates. Alongside this assumption, as well as that ice temperatures are steady, and that the thermal diffusivity is spatially constant, the equation (2) reduces to

$$\nabla \cdot (\mathbf{u}T) = \kappa \frac{\partial^2 T}{\partial z^2} \tag{3}$$

where $\mathbf{u}$ is the ice velocity. Taking x to be everywhere locally parallel to the flow and y everywhere local perpendicular to the flow, and assuming that the flow is incompressible, equation (2) reduces to

$$u\frac{\partial T}{\partial x} + w\frac{\partial T}{\partial z} = \kappa \frac{\partial^2 T}{\partial z^2} \tag{4}$$

where u and w components of velocity in the x and z directions, respectively.

Equation (4) is that considered by (Sergienko et al., 2013). They show that for a large Peclet number, $Pe = H^2 u/(L\kappa) \gg 1$, where H is the ice thickness, and L the lengthscale of the flow, the solution to (4) on floating ice shelves may be expressed as

$$T(x, \hat{z}) = T_g\left[\xi(x, \hat{z})\right] + \left\{T^*(x) - T_g\left[\xi(x, 0)\right]\right\} \exp\left(-\frac{\hat{z}}{\ell}\right) \tag{5}$$

where $\hat{z} = z/H$ is a dimensionless vertical co-ordinate, $H = H(x)$ is the local ice thickness, $\ell = \kappa/(\dot{m}H)$ is the lengthscale of the boundary warming effect, with $\dot{m}$ the local melt rate, $T^*(x)$ is the local freezing temperature, T_g the temperature profile at the grounding line, and

$$\xi(x, \hat{z}) = 1 - \frac{1 - \hat{z}}{g_q} q(x), \tag{6}$$

where $q(x) = u(x)H(x)$ is the ice flux, and q_g is the ice flux at the grounding line. The solution (5) results from assuming that surface accumulation is negligible, but is shown in (Sergienko et al., 2013) to make little difference to the temperature profile. Note that in the case of a negative basal melt rate (i.e. basal freezing) the temperature profile (5) predicts a temperature which grows exponentially away from the ice-ocean interface, which

is clearly unphysical. To avoid this scenario, negative melt rates observed in practice are set to a small positive value (see below).

Following (Sergienko et al., 2013), we take the grounding line temperature profile from (Robin, 1955),

$$T_g(\hat{z}) = T_s - \frac{Q}{K}\sqrt{\frac{2H_g\kappa}{\dot{A}}}\left[\operatorname{erf}\left(\sqrt{\frac{\dot{A}H_g}{2\kappa}}\right) - \operatorname{erf}\left(\sqrt{\frac{\dot{A}\hat{z}^2H_g}{2\kappa}}\right)\right] \tag{7}$$

where T_s is the surface temperature, Q is the geothermal heat flux per unit area, K is the thermal conductivity of ice, H_g is the ice thickness at the grounding line, $\dot{A}$ is the surface accumulation, and $\operatorname{erf}(\phi) = \int_0^\phi \exp(-\lambda^2)\,\mathrm{d}\lambda$ is the error function. The temperature profile (7) is based on a balance between diffusion through the ice column, which is geothermally heated at its base, and cold surface temperatures, and is appropriate for plug flow with no strain heating effects. Ideally, we would have an approximation which includes these effects, particularly as ice advection is so important, but no analytic solution to the heat equation exists under these constraints.

The temperature profile (5) requires the ice flux to be known everywhere along a flowline. This is problematic when determining collapse timescales because we have no way to determine the velocity response to thinning, which requires the use of an ice sheet model. To alleviate this problem, we make an 'unconfined ice shelf' approximation, setting the local ice flux equal to the grounding line flux. In this case, $\xi = \hat{z}$ and the temperature profile (5) reduces to

$$T(x,\hat{z}) = T_g(\hat{z}) + \{T^*(x) - T_g\left[\xi(x,\hat{z})\right]\}\exp\left(-\frac{\hat{z}}{\ell}\right). \tag{8}$$

In figure 6, we show a comparison between the temperature profile (5) and the approximation (8) to it for flowlines taken along the Ross and Pine Island ice shelves (i.e. those shown in figure 1a). These solutions demonstrate that the approximation works well, capturing the key features, with relatively small errors (figure 6e–f). The decoupling from the ice flux within the shelf can be seen particularly for the low basal melt rate profile (figure 6a), for which the temperature is more clearly advected downstream. Our approximation has the benefit that it does not require the velocity to be defined, allowing us to extend temperature profiles to areas with missing velocity data, such as at ice fronts (compare figure 6b and d, for example). In general, on ice shelves with low basal melt rates, the approximation (8) overestimates ice temperatures in some regions and underestimates in others, compared to (5) (figure 6e). For ice shelves with high basal melt rates,

the (8) systematically overestimates temperatures (figure 6f). This is because, in high basal melt rate ice shelves, the flux reduces downstream owing to stronger reductions in ice thickness; when the flux is reduced downstream ($q(x)/q_g$ reduces downstream, so ξ increases) as it is in practice, the surface, where $\xi = 1$ and temperatures are colder, has a great contribution.

Determining the crevassing timescales

For a given ice column thickness, strain rate, thinning rate, and basal melt rate, the crevassing timescale is computed by timestepping the thickness according to the thinning rate, and at each timestep, updating the temperature profile from (8) and determining the crevasse depth according to the LEFM (see 'Linear elastic fracture mechanics theory' below). If the thinning rate is positive (i.e. the column of ice is getting thinner with time), the dimensionless crevasse depth will increase in time, and the crevassing timescale is taken to be the first time at which the crevasse propagates through the entire column of ice, where $d_C/H = 1$. In the results shown here, ice thickness updates have a timestep of a 1 year timestep, which effectively sets the resolution of the results. If the thinning rate is negative, the crevasse depth decreases in time, and the situation is more complicated: if the dimensionless crevasse depth is one prior to any thinning, the crevassing timescale is 0; if the dimensionless crevasse depth is less than one at the start of the simulation, the crevassing timescale is not defined. The crevassing timescale is also not defined in regions with negative strain rates because in these regions, LEFM necessarily predict zero crevasse depth (see below).

In all results shown here, we assume a constant basal temperature of -2 °C. In practice, ice shelf basal temperatures are necessarily at the local freezing temperature, which in general has a dependence on both salinity and depth; accurately determining the ice shelf basal temperature would therefore require us to determine the salinity at the ice-ocean interface, which is only achievable through the use of a coupled-ice ocean model and is beyond the scope of this work. However, depth and salinity dependence on basal melt rates are fairly weak, justifying our use of a constant value. This constant value agrees well with observation constraints on the Amery ice shelf (supplementary figure 7). To isolate the effects of basal melting on temperature profiles, we also assume other several other quantities entering into the temperature profiles are constant. In particular, we assume a constant surface temperature $T_s = -22$ °C, a constant geothermal heat flux

$Q = 48$ W/m^2, and accumulation rate $\dot{A} = 0.1$ m a^{-1}. We take a constant ice fracture toughness $K = 150$ kPa and non-linear viscous ice rheology, taking a Glen flow law with Glen's flow exponent $n = 3$.

Antarctic collapse timescales

To construct the map of circum-Antarctic crevassing timescales, we assimilate melt rate data (supplementary figure 10e) from (Adusumilli et al., 2020), thinning rate data (supplementary figure 10a) from (Smith et al., 2020), ice thickness data (supplementary figure 10d) from Bedmap v2 (Fretwell et al., 2013) and strain rate data from [Wearing] (supplementary figure 10c). Coverage of Antarctic ice shelves – defined as the proportion of ice shelf points in the Bedmap datasat which have a well-defined thinning rate, strain rate, and melt rate – is 82%. Much of the data gap arises from the melt rate product, highlighting the need for continued improvement in basal melt rate products, in particular.

Melt rate data is used to determine the ice temperature profiles, which set the ice viscosity (see 'Linear elastic fracture mechanics theory'). Since the temperature profile is not well-defined for negative melt rates (see 'Ice shelf temperature profiles'), we set the melt rate on all grid points with a negative melt to be 0.1 m year^{-1} (supplementary figure 10f). This adjustment does not affect melt rates on warm water ice shelves with high basal melt rates, but is relevant for cold water ice shelves. We expect that adjusting the melt rate in this way would increase the modelled ice temperature (relative to actual), as a positive basal melt rate reflects a source of heat into the ice. Thus, modelled ice temperatures on low melt rate ice shelves may be warmer than they are in practice, suggesting that crevasse timescales reported here may be longer than they should be on these shelves. When compared with borehole estimates on the Amery Ice Shelf, which is associated with low basal melt rates, modelled temperatures are indeed typically larger than observed temperatures (supplementary figure 8).

Ice shelf thinning rates from (Smith et al., 2020) are used to determine ice shelf thinning over each time step. The pattern of ice shelf thinning rates (supplementary figure 10a) is highly spatially heterogeneous and features large errors (Smith et al., 2020), which dominate the signal in places. In addition, the crevassing timescale is not defined in locations with positive thinning rates. To work around these issues, we use a constant thinning

rate on each ice shelf (supplementary figure 10b). We take this constant value to be one standard deviation above the mean thinning rate measured at all grid points on the ice shelf. This measure respects the fact that the thinning rate from (Smith et al., 2020) is an average over 2003–2019, over which time thinning of many ice shelves has accelerated (Smith et al., 2020). According to this measure, all ice shelves, except for an isolated region in Dronning Maud Land, have a positive thinning rate. The dataset of (Smith et al., 2020) is provided on a 5km grid and downscaled using a linear interpolation.

Linear elastic fracture mechanics theory

The background of LEFM applied to ice shelves is presented in detail in the supplementary information of (Lai et al., 2020). Here, we provide a brief overview. In the LEFM framework for basal crevasses, crevasse depths are determined by considering three stresses: the background resistive stress in the ice shelf, the water pressure within basal crevasses, and the weight of the ice (supplementary figure 8). When the ice shelf is in tension (positive strain rates), background resistive stresses act to open basal crevasses, while, when in compression (negative strain rates), background resistive stresses act to close basal crevasses. The water pressure within basal crevasses is higher than the neighbouring hydrostatic ice pressure, which additionally encourages crack growth. The weight of ice acts to close crevasses, discouraging their propagation. In LEFM, the concentration of stresses near the crevasse tip is expressed as a mode I stress intensity factor, which depends on the stress distribution K_{IC} acting on the fracture surfaces. Since the framework is linear, this stress intensity can be expressed as the superposition of terms corresponding to the three components, which vary with the crevasse depth d,

$$K_{IC} = K_{IC}(d) = K_R(d) + K_W(d) - K_I(d). \tag{9}$$

The terms on the right-hand side of (9) correspond to tensile resistive stresses, water pressure, and the weight of water, respectively, and are shown schematically as a function of depth in supplementary figure 8.

To determine the crevasse depth d predicted by LEFM, the stress intensity (9) is compared with the fracture toughness of ice (a material property), denoted K. Crevasses may propagate to the depth d at which the stress intensity K_{IC} equals the fracture toughness K; however, these depths only correspond to stable configurations when the stress intensity decreases with increasing crevasse depth (supplementary figure 8), and vice versa:

368 if the stress intensity K_{IC} increases with crevasse depth, it is energetically favourable
369 for the crack to grow (supplementary figure 8); it is this stable, physically relevant crevasse
370 depth which is reported here.

The tensile resistive stress term can be expressed as

$$K_R = \int_0^{\frac{d}{H}} \frac{2R_x x(\hat{z})\sqrt{\pi d}}{G}\left(\hat{z}, \frac{d}{H}\right)\left[1 - \frac{d}{H}\right]^{-3/2}(1-\hat{z})^{-1/2}\,\mathrm{d}z \tag{10}$$

where H is the ice thicknessand G a dimensionless weight function whose analytic form can be found in (Tada et al., 1973). R_{xx} is the resistive stress (C. Van der Veen, 1998; C. J. Van der Veen, 2013),

$$R_x x = 2B(T(z))\epsilon_{xx}|\epsilon_{xx}|^{1/n-1}, \tag{11}$$

where $B(T(z))$ is the ice viscosity, with $T(z)$ the depth-dependent temperature profile, ϵ_{xx} is the strain rate and n is Glen's flow exponent. The ice viscosity $B(T)$ is expressed using a common Arrhenius type relationship (LeB. Hooke, 1981)

$$B(T(z)) = B_0 \exp\left[\frac{T}{T_0} - \frac{C}{(T_r - T)^k}\right] \tag{12}$$

371 where $B_0 == 1.928 \times 10^{-5}$ bar $\mathrm{a}^{1/3}$, $T_0 = 3155$ K, $C = 0.11612$ $\mathrm{K}^1.17$, and $T_r =$
372 273.39 K. As the temperature increases, the $B(T)$ decreases, making the resistive stress
373 R_{xx}, and thus the stress intensity component K_R smaller.

The other terms in (9) are

$$K_W(d) = \frac{2\rho_w g d^{3/2}}{\sqrt{\pi}} g_b(d) \tag{13}$$

$$K_I(d) = \frac{2\rho_i g d^{3/2}}{\sqrt{\pi}} f_b(d) \tag{14}$$

where $\rho_w = 1028.0$ kg m^{-3} and $\rho_i = 918.0$ kg m^{-3} are the densities of seawater and ice, respectively, $g = 9.81$ m s^{-2} is the acceleration due to gravity, and f_b and g_b are dimensionless weight functions

$$g_b(d) = \int_0^1 \left(\frac{\rho_i}{\rho_w}\frac{H}{d} - \hat{z}\right) G\left(\hat{z}, \frac{d}{H}\right)\left(1 - \frac{d}{H}\right)^{-3/2}(1-\hat{z}^2)^{-1/2}\,\mathrm{d}\hat{z}, \tag{15}$$

$$f_b(d) = \int_0^1 \left(\frac{H}{d} - \hat{z}\right) G\left(\hat{z}, \frac{d}{H}\right)\left(1 - \frac{d}{H}\right)^{-3/2}(1-\hat{z}^2)^{-1/2}\,\mathrm{d}\hat{z}. \tag{16}$$

Supplementary Figures

References

Adusumilli, S., Fricker, H. A., Medley, B., Padman, L., & Siegfried, M. R. (2020). Interannual variations in meltwater input to the southern ocean from antarctic ice shelves. *Nature geoscience*, *13*(9), 616–620. (Used as dataset for basal melt rates)

Bett, D. T., Bradley, A. T., Williams, C. R., Holland, P. R., Arthern, R. J., & Goldberg, D. N. (2023). Coupled ice/ocean interactions during the future retreat of west antarctic ice streams. *The Cryosphere Discussions*, *2023*, 1–28.

Bradley, A., Bett, D., Dutrieux, P., De Rydt, J., & Holland, P. (2022). The influence of pine island ice shelf calving on basal melting. *Journal of Geophysical Research: Oceans*, *127*(9), e2022JC018621.

Bradley, A. T., De Rydt, J., Bett, D. T., Dutrieux, P., & Holland, P. R. (2023). The ice dynamic and melting response of pine island ice shelf to calving. *Ann. Glac.*, 1–5.

Coffey, N., Lai, C.-Y., & Wang, Y. (2023). *Rift initiation via unstable basal crevasses* (Tech. Rep.). Copernicus Meetings.

Coulon, V., Klose, A. K., Kittel, C., Edwards, T., Turner, F., Winkelmann, R., & Pattyn, F. (2023). Disentangling the drivers of future antarctic ice loss with a historically-calibrated ice-sheet model. *EGUsphere*, *2023*, 1–42.

DeConto, R. M., & Pollard, D. (2016). Contribution of antarctica to past and future sea-level rise. *Nature*, *531*(7596), 591–597.

DeConto, R. M., Pollard, D., Alley, R. B., Velicogna, I., Gasson, E., Gomez, N., ... others (2021). The paris climate agreement and future sea-level rise from antarctica. *Nature*, *593*(7857), 83–89.

Edwards, T. L., Nowicki, S., Marzeion, B., Hock, R., Goelzer, H., Seroussi, H., ... others (2021). Projected land ice contributions to twenty-first-century sea level rise. *Nature*, *593*(7857), 74–82. doi: 10.1038/s41586-021-03302-y

Eicken, H., Oerter, H., Miller, H., Graf, W., & Kipfstuhl, J. (1994). Textural characteristics and impurity content of meteoric and marine ice in the ronne ice shelf, antarctica. *Journal of Glaciology*, *40*(135), 386–398.

Fisher, A. T., Mankoff, K. D., Tulaczyk, S. M., Tyler, S. W., Foley, N., & Team, W. S. (2015). High geothermal heat flux measured below the west antarctic ice

sheet. *Science advances*, *1*(6), e1500093.

Fretwell, P., Pritchard, H. D., Vaughan, D. G., Bamber, J. L., Barrand, N. E., Bell, R., ... others (2013). Bedmap2: improved ice bed, surface and thickness datasets for antarctica. *The Cryosphere*, *7*(1), 375–393.

Fürst, J. J., Durand, G., Gillet-Chaulet, F., Tavard, L., Rankl, M., Braun, M., & Gagliardini, O. (2016). The safety band of antarctic ice shelves. *Nature Climate Change*, *6*(5), 479–482. doi: 10.1038/nclimate2912

Grosfeld, K., & Thyssen, F. (1994). Temperature investigation and modeling on the filchner-ronne ice shelf, antarctica. *Annals of Glaciology*, *20*, 377–385.

Gudmundsson, G. H., Barnes, J. M., Goldberg, D., & Morlighem, M. (2023). Limited impact of thwaites ice shelf on future ice loss from antarctica. *Geophysical Research Letters*, *50*(11), e2023GL102880.

Gudmundsson, G. H., Krug, J., Durand, G., Favier, L., & Gagliardini, O. (2012). The stability of grounding lines on retrograde slopes. *The Cryosphere*, *6*(6), 1497–1505. Retrieved from `https://tc.copernicus.org/articles/6/1497/2012/` doi: 10.5194/tc-6-1497-2012

Kobs, S., Holland, D. M., Zagorodnov, V., Stern, A., & Tyler, S. W. (2014). Novel monitoring of antarctic ice shelf basal melting using a fiber-optic distributed temperature sensing mooring. *Geophysical Research Letters*, *41*(19), 6779–6786.

Lai, C.-Y., Kingslake, J., Wearing, M. G., Chen, P.-H. C., Gentine, P., Li, H., ... van Wessem, J. M. (2020). Vulnerability of antarctica's ice shelves to meltwater-driven fracture. *Nature*, *584*(7822), 574–578. doi: 10.1038/s41586-020-2627-8

LeB. Hooke, R. (1981). Flow law for polycrystalline ice in glaciers: Comparison of theoretical predictions, laboratory data, and field measurements. *Reviews of Geophysics*, *19*(4), 664-672. doi: https://doi.org/10.1029/RG019i004p00664

Lhermitte, S., Sun, S., Shuman, C., Wouters, B., Pattyn, F., Wuite, J., ... Nagler, T. (2020). Damage accelerates ice shelf instability and mass loss in amundsen sea embayment. *Proc. Natl. Acad. Sci. U.S.A*, *117*(40), 24735–24741.

Liu, Y., Moore, J. C., Cheng, X., Gladstone, R. M., Bassis, J. N., Liu, H., ... Hui, F. (2015). Ocean-driven thinning enhances iceberg calving and retreat of antarctic ice shelves. *Proceedings of the National Academy of Sciences*,

112(11), 3263–3268.

Marsh, O. J., Luckman, A. J., & Hodgson, D. A. (2023). Brief communication: Rapid acceleration of the brunt ice shelf after calving of iceberg a-81. *EGUsphere*, 1–9.

Naughten, K. A., De Rydt, J., Rosier, S. H., Jenkins, A., Holland, P. R., & Ridley, J. K. (2021). Two-timescale response of a large antarctic ice shelf to climate change. *Nature communications*, *12*(1), 1991.

Nicholls, K. (1997). Predicted reduction in basal melt rates of an antarctic ice shelf in a warmer climate. *Nature*, *388*(6641), 460–462.

Nye, J. F. (1957). The distribution of stress and velocity in glaciers and ice-sheets. *Proceedings of the Royal Society of London. Series A. Mathematical and Physical Sciences*, *239*(1216), 113–133.

Park, J.-Y., Schloesser, F., Timmermann, A., Choudhury, D., Lee, J.-Y., & Nellikkattil, A. B. (2023). Future sea-level projections with a coupled atmosphere-ocean-ice-sheet model. *Nature Communications*, *14*(1), 636.

Reese, R., Gudmundsson, G. H., Levermann, A., & Winkelmann, R. (2018). The far reach of ice-shelf thinning in antarctica. *Nat Clim Chang.*, *8*(1), 53–57. doi: 10.1038/s41558-017-0020-x

Robel, A. A., & Banwell, A. F. (2019). A speed limit on ice shelf collapse through hydrofracture. *Geophysical Research Letters*, *46*(21), 12092–12100.

Robin, G. d. Q. (1955). Ice movement and temperature distribution in glaciers and ice sheets. *Journal of glaciology*, *2*(18), 523–532.

Sergienko, O., Goldberg, D., & Little, C. (2013). Alternative ice shelf equilibria determined by ocean environment. *Journal of Geophysical Research: Earth Surface*, *118*(2), 970–981.

Seroussi, H., Nowicki, S., Payne, A. J., Goelzer, H., Lipscomb, W. H., Abe-Ouchi, A., ... others (2020). Ismip6 antarctica: a multi-model ensemble of the antarctic ice sheet evolution over the 21st century. *The Cryosphere*, *14*(9), 3033–3070.

Smith, B., Fricker, H. A., Gardner, A. S., Medley, B., Nilsson, J., Paolo, F. S., ... Zwally, H. J. (2020). Pervasive ice sheet mass loss reflects competing ocean and atmosphere processes. *Science*, *368*(6496), 1239–1242. (Used as dataset for thinning rate)

Sun, S., Cornford, S. L., Moore, J. C., Gladstone, R., & Zhao, L. (2017). Ice shelf fracture parameterization in an ice sheet model. *The Cryosphere*, *11*(6), 2543–2554.

Sun, S., Pattyn, F., Simon, E. G., Albrecht, T., Cornford, S., Calov, R., ... others (2020). Antarctic ice sheet response to sudden and sustained ice-shelf collapse (abumip). *Journal of Glaciology*, *66*(260), 891–904. doi: 10.1017/jog.2020.67

Tada, H., Paris, P. C., & Irwin, G. R. (1973). The stress analysis of cracks. *Handbook, Del Research Corporation*, *34*(1973).

Tyler, S., Holland, D., Zagorodnov, V., Stern, A., Sladek, C., Kobs, S., ... Bryenton, J. (2013). Using distributed temperature sensors to monitor an antarctic ice shelf and sub-ice-shelf cavity. *Journal of Glaciology*, *59*(215), 583–591.

Van der Veen, C. (1998). Fracture mechanics approach to penetration of bottom crevasses on glaciers. *Cold Regions Science and Technology*, *27*(3), 213–223.

Van der Veen, C. J. (2013). *Fundamentals of glacier dynamics*. CRC press.

Wang, Y., Zhao, C., Gladstone, R., Galton-Fenzi, B., & Warner, R. (2022). Thermal structure of the amery ice shelf from borehole observations and simulations. *The Cryosphere*, *16*(4), 1221–1245.

Zarrinderakht, M., Schoof, C., & Peirce, A. (2022). The effect of hydrology and crevasse wall contact on calving. *The Cryosphere*, *16*(10), 4491–4512.

Zarrinderakht, M., Schoof, C., & Peirce, A. (2023). An analysis of the interaction between surface and basal crevasses in ice shelves. *EGUsphere*, *2023*, 1–21.

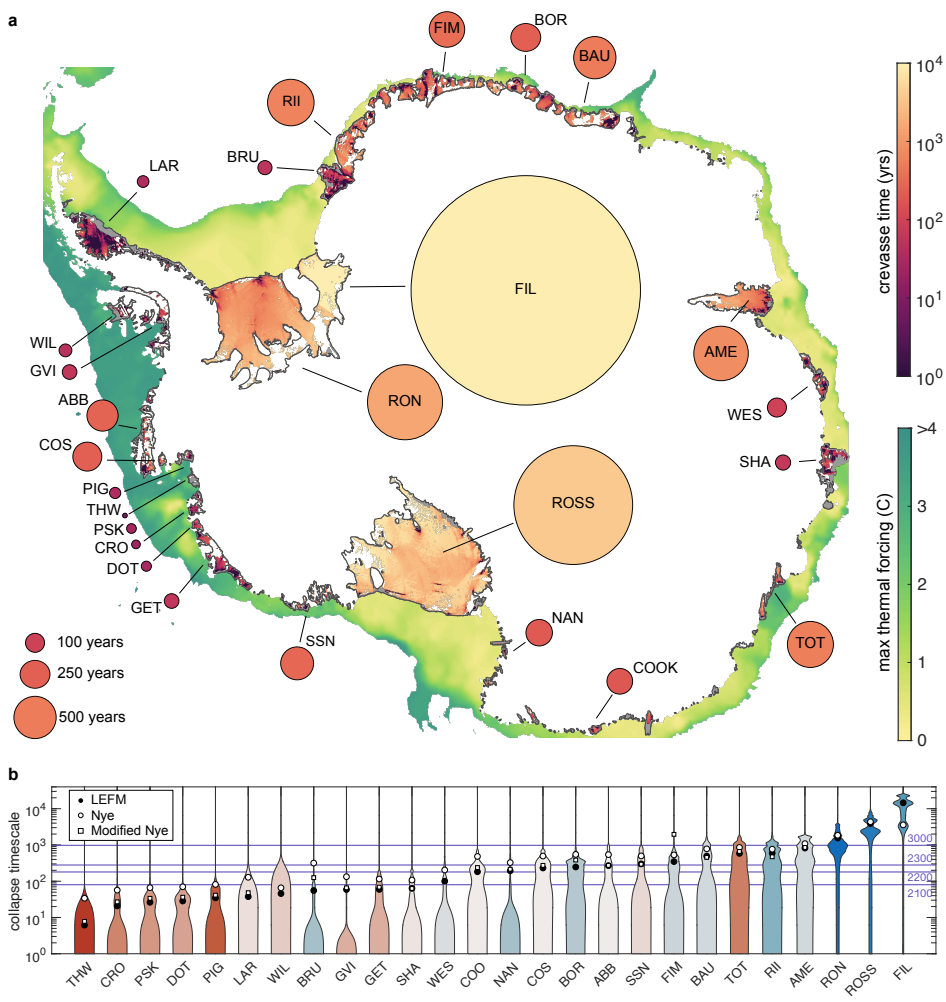

Figure 3. Collapse timescales of Antarctic ice shelves. (a) Circum-Antarctic crevassing timescales shown as colours in the yellow-red-black colormap. Ice shelf locations with missing data are shown in grey. Ocean thermal forcing from ref. (Adusumilli et al., 2020) are shown in the yellow-green colormap. Circles show collapse timescales, indicated by both the area of the circle, which is proportional to the collapse timescale, and its colour, which corresponds to the crevasse time colorbar. (b) Distributions of crevassing times for major Antarctic ice shelves shown as violin plots. For each, the black dot indicates the collapse timescale for that shelf, computed as the mean of the kernel density estimate, while the white circle and white square respectively indicate the collapse timescales obtained using a crevasse depth determined by Nye theory (Nye, 1957) and modified Nye theory (Coffey et al., 2023), rather than LEFM (methods). Shelves are ordered in order of increasing LEFM collapse timescale. Note that the ordinate axis in this plot is logarithmic, and so it appears that the mean of the black dots is weighted towards higher crevassing times than it would on a linear axis. Background lines indicate the time to 2100, 2200, 2300 and 3000, as labelled.

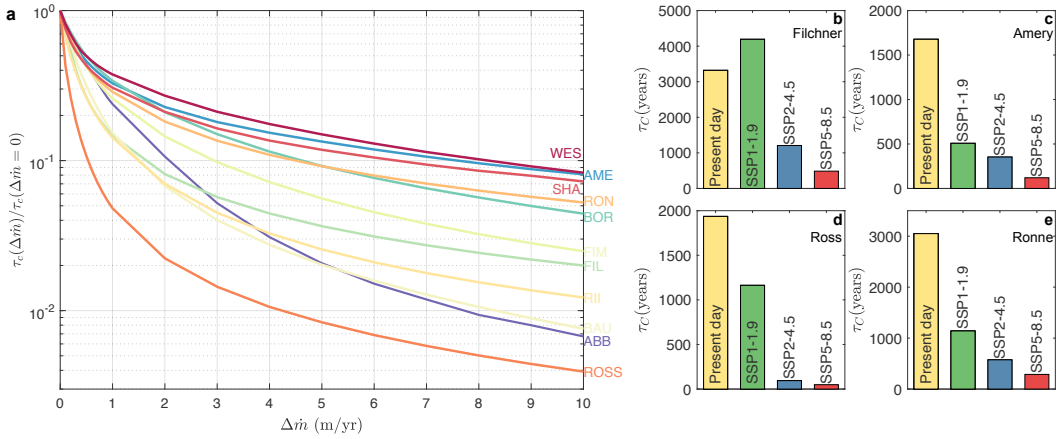

Figure 4. High sensitivity of collapse timescales to future increases in basal melting. (a) Semilog plot of collapse timescale as a function of $\Delta\dot{m}$, a uniform increase in basal melt rate applied everywhere on the shelf. (b)–(e) Collapse timescales of major ice shelves under different SSP scenarios at the year 2100, with $\Delta\dot{m}$ values computed from basal melt rates in coupled ice-ocean-atmosphere simulations (Park et al., 2023) (methods). Each panel corresponds to a different scenario, as labelled.

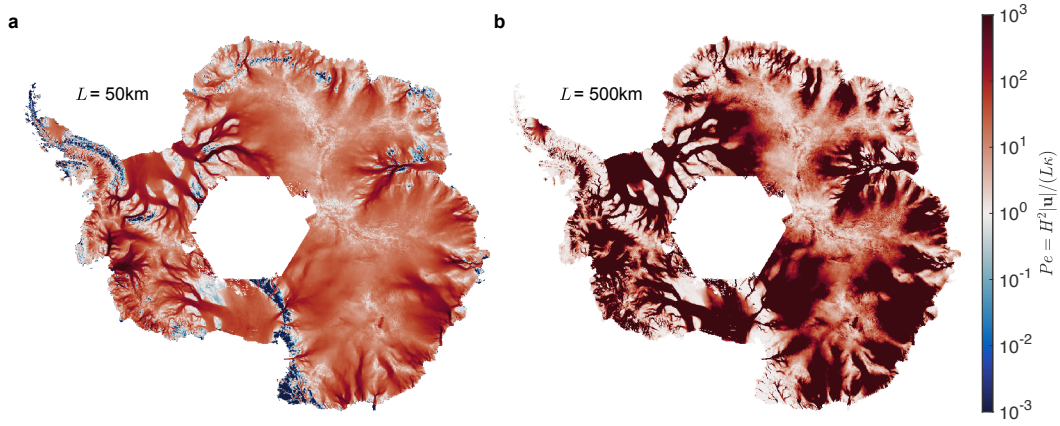

Figure 5. Advection dominates heat transfer within the Antarctic ice sheet. Maps of Peclet number $Pe = H^2|\mathbf{u}|/(L\kappa)$, where H is the ice thickness, $\mathbf{u}$ is the velocity, κ is the ice thermal diffusivity, and L is a flow lengthscale. Maps are shown for (a) a lengthscale $L = 50$ km and (b) a lengthscale $L = 500$ km. Red areas indicate regions where advection dominates over diffusion.

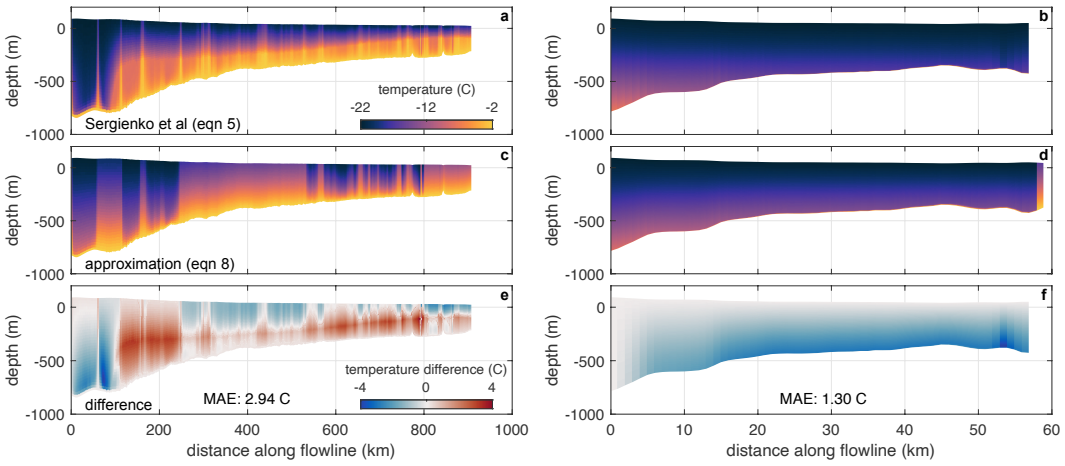

Figure 6. Comparison between ice shelf temperature profiles. Temperature profiles along a flowline on (a, c) the Ross ice shelf and (b, d) the Pine Island ice shelf. In both cases, the top row (i.e. panels a–b) indicates the solution (5) from (Sergienko et al., 2013) and the second row (panels c–d) indicates the approximation (8). The colorbar in (a) is relevant for each of (a)–(d). Note that the temperature profile is not defined in (b) for flowline distances beyond 57km because the ice velocity observations are missing in this region. (e,f) Differences between the approximations, i.e. the difference between panels (a) and (c), and (b) and (d), respectively. In red (blue, respectively) areas, the flux-independent approximation underestimates (overestimates) the temperature. The colorbar in (e) is relevant for both (e) and (f).

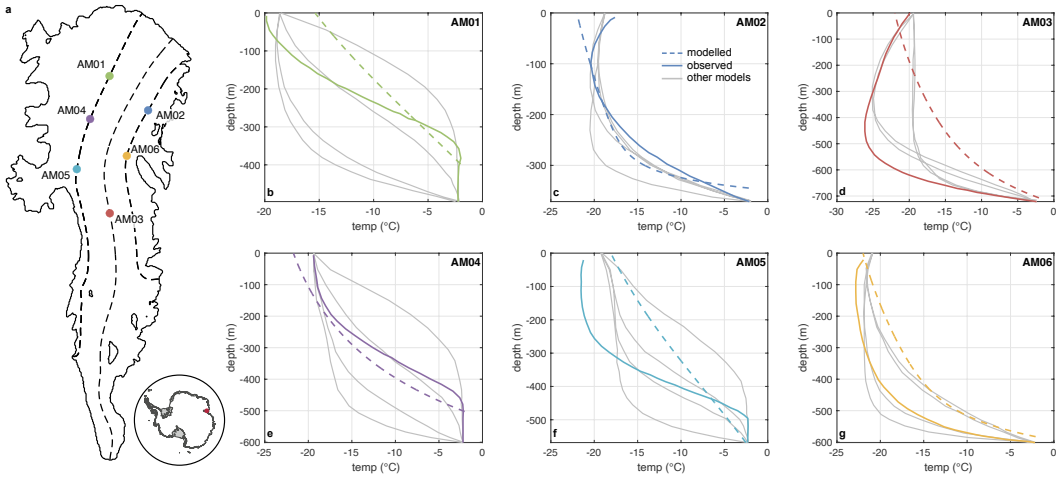

Figure 7. Modelled and observed borehole temperatures on the Amery ice shelf. (a) Outline of the Amery ice shelf, with three flowlines (dashed lines) along which boreholes AM01–AM06 from (Wang et al., 2022) are located, as marked. The inset shows the location of the Amery ice shelf within Antarctica. (b)–(g) Modelled (equation (8), dashed lines) and observed (solid lines, from (Wang et al., 2022) temperatures at borehole locations AM01–AM06, as indicated in panel (a). Also shown as grey curves are modelled temperature profiles from (Wang et al., 2022) using a thermomechanically-coupled, full-Stokes ice sheet model; each curve corresponds to a different basal mass balance product.

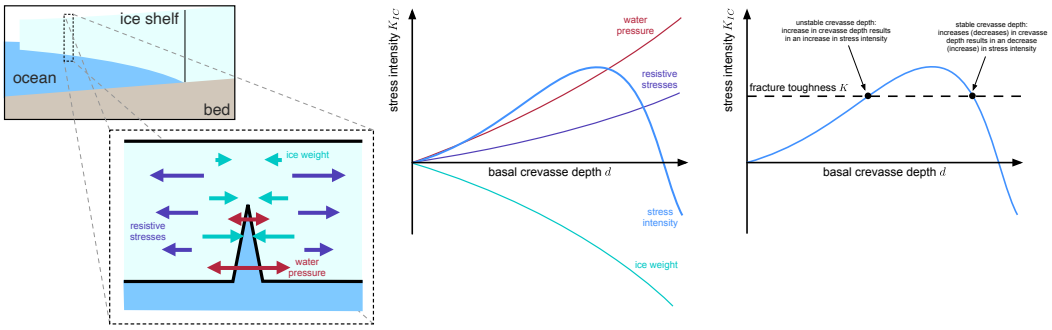

Figure 8. Linear elastic fracture mechanics framework.

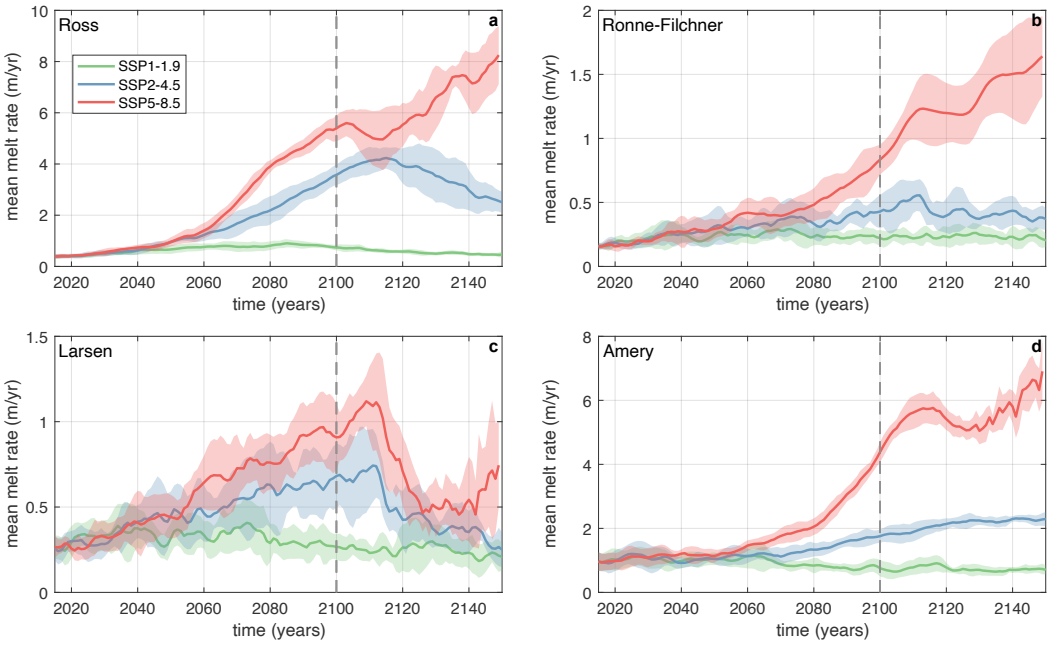

Figure 9. Ice shelf melt rates in coupled ice-ocean-atmosphere simulations. Each panel shows the evolution of the 10 member ensemble mean (solid lines) and standard deviation (shaded region) of melt rates on ice shelves from (Park et al., 2023), with each panel corresponding to a different ice shelf as labelled. Different colours correspond to different emissions scenarios as follows: SSP1-1.9 (green), SSP2-4.5 (blue) and SSP5-8.5 (red).

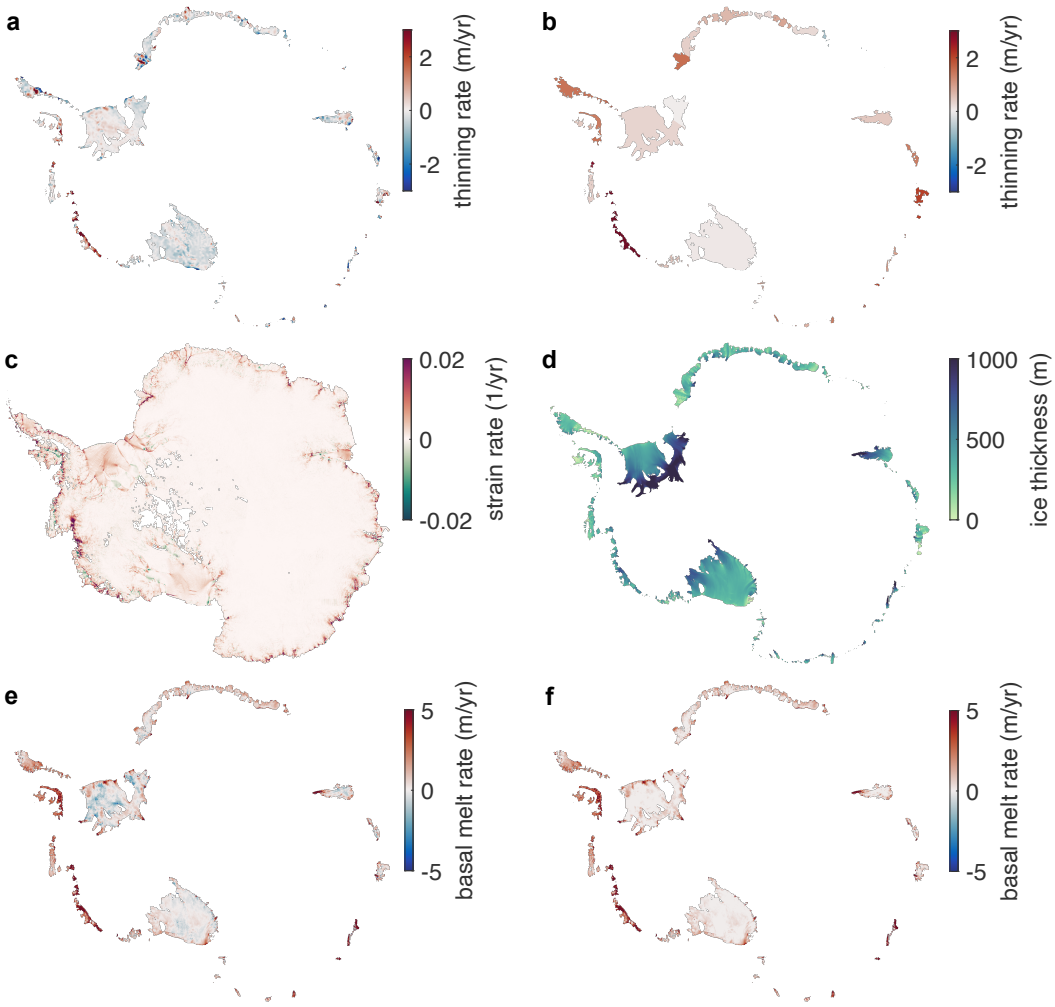

Figure 10. Datasets used in the calculation of circum-Antarctic crevassing times. (a) thinning rate from (Smith et al., 2020), and (b) shelf averaged thinning rates (methods). (c) Strain rates from Wearing. (d) Ice thickness from Bedmap2 (Fretwell et al., 2013), (e) basal melt rates from (Adusumilli et al., 2020) and (f) ad-hoc adjusted melt rates used in the calculation (methods).

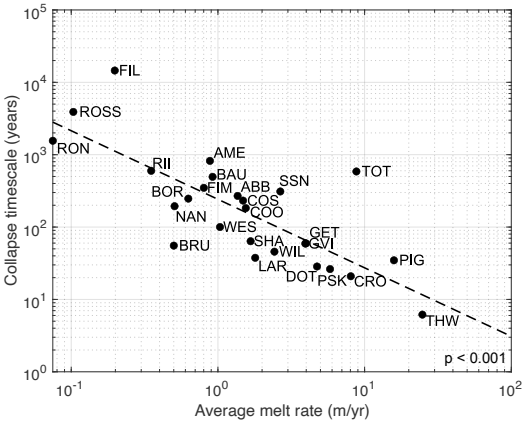

Figure 11. Scatter plot of average basal melt rate against collapse timescale for Antarctic ice shelves. The black dashed line indicates the best linear fit to the log of the quantities (note that this appears as a straight on the logarithmic axes).